AUTONOMOUS NAVIGATION AROUND DIDYMOS USING CNN-BASED IMAGE PROCESSING

Aurelio Kaluthantrige[*], Iosto Fodde[†], Jinglang Feng[‡] and Jesús Gil-Fernández[§]

HERA is an asteroid rendezvous mission of the European Space Agency (ESA) that will investigate the binary asteroid system (65803) Didymos. The proximity operations of HERA's spacecraft around the target body rely on an autonomous optical navigation system that collects on-board visual information to estimate the relative position and attitude of the spacecraft with respect to the asteroid. The core component of this navigation method is the Image Processing (IP) algorithm that extracts optical observables from images captured by the spacecraft's on-board Asteroid Framing Camera (AFC). The Early Characterization Phase (ECP) is a proximity operation of HERA with the objective of conducting physical and dynamical characterizations of Didymos. This paper develops a pipeline to estimate the position of HERA spacecraft around binary asteroid system Didymos during the ECP using a Convolutional Neural Networks (CNN)-based IP algorithm. The proposed algorithm uses the images captured with the AFC camera to estimate the pixel position of the centroid of Didymos and the pixel position of a set of keypoints on the visible border of Didymos. With these points, the algorithm evaluates the apparent radius of the primary, which is used to measure the pseudorange by applying the pinhole camera model. Subsequently, the algorithm combines the measured centroid and pseudorange with an Unscented Kalman Filter (UKF) to estimate the relative position of the spacecraft. The training, validation and testing datasets are generated with the software Planet and Asteroid Natural scene Generation Utility (PANGU). The High-Resolution Network (HRNet) is used as CNN architecture as it represents the state-of-the-art technology in keypoint detection. The HRNet-based IP algorithm measures the pseudorange and estimates the position of the centroid with high accuracy. The UKF is able to process the centroid and pseudorange measurements to produce an accurate state estimate with an error of around $300\ m$ and $2\ cm/s$.

INTRODUCTION

The Asteroid Impact Deflection Assessment (AIDA) is an international collaboration between the National Aeronautics and Space Administration (NASA) and the European Space Agency (ESA), with the primary objective of investigating a binary asteroid system and to demonstrate its deflection by kinetic impact. The NASA contribution to this mission is the Double Asteroid Redirection Test (DART), a kinetic impactor launched on the 24th of November 2021 that will perform the

---

[*]Ph. D. Candidate, Department of Mechanical and Aerospace Engineering, University of Strathclyde, 75 Montrose Street, Glasgow G1 1XJ, United Kingdom, mewantha.kaluthantrige-don@strath.ac.uk

[†]Ph. D. Candidate, Department of Mechanical and Aerospace Engineering, University of Strathclyde, 75 Montrose Street, Glasgow G1 1XJ, United Kingdom

[‡]Lecturer, Department of Mechanical and Aerospace Engineering, University of Strathclyde, 75 Montrose Street, Glasgow G1 1XJ, United Kingdom

[§]Guidance, Navigation and Control engineer, ESTEC, ESA, Keplerlaan 1, 2200 AG Noordwijk, The Netherlands

deflection in September 2022.[1] ESA's segment of the AIDA mission is represented by HERA, whose objectives are to research the properties of the binary asteroid system, to observe the results of DART's impact and to assess the feasibility of the deflection technique.[2] HERA falls under ESA's Space Situational Awareness (SSA) initiative, which enables ESA to detect, predict and assess the risk of Near Earth Objects.

The target of this mission is the near-Earth asteroid (65803) Didymos and its moon Dimorphos. Table 1 illustrates relevant properties of Didymos and Dimorphos. The spin axis of both bodies is orthogonal to the binary's orbital plane. Dimorphos is tidally locked with Didymos, i.e. its rotation period is equal to its revolution period around the primary.[3] The proximity operations of HERA

Table 1: Didymos' system properties[3]

Parameter	Didymos	Dimorphos
Gravitational parameter (km^3/s^2)	$3.5225 \cdot 10^{-8}$	$2 \cdot 10^{-10}$
Diameter (m)	780	164
Rotation period ($hours$)	2.26	11.92
Obliquity of the binary orbit with Ecliptic plane	$169.2°$	$169.2°$

consist of different phases that depend on the mission objectives. The focus of this work is the Early Characterization Phase (ECP), with the spacecraft at a distance of around $30\ km$ from the target with the objective of conducting physical and dynamical characterizations of Didymos.[4]

Observing a binary asteroid system from such a short distance is unprecedented. A vision based Guidance, Navigation and Control (GNC) system is designed to improve the mission autonomy. This system comprises an on-board camera taking images of the asteroid, an Image Processing (IP) algorithm that extracts information from these images, and a navigation filter that is able to process the visual data to estimate the spacecraft position, velocity and attitude with respect to the binary system. The camera used for the vision based navigation system is the Asteroid Framing Camera (AFC). For the ECP, the navigation strategy is centroid-based, meaning that the IP algorithm is designed to extract the Center of Mass (COM) of the primary body, thus estimating the Line Of Sight of the spacecraft, with the purpose of enabling autonomous attitude navigation.[5] Nevertheless, standard IP algorithms' performances are highly depending on the intrinsic properties of the captured images. Factors such as the Signal-to-Noise ratio, illumination conditions, the presence of other bodies in the image and the irregular shape of the asteroid can affect the accuracy of the extracted visual information.

To estimate the relative position of the spacecraft, range measurements with the asteroid are required. The on-board instrument to measure the range with Didymos is the Planet ALTimeter (PALT), a lidar experiment that determines the distance to the asteroids with an accuracy of 0.5 m by measuring the time of flight of a laser beam at $1.5\ \mu m$ wavelength. PALT is operational at a distance ranging from $500\ m$ to $14\ km$, hence it cannot be used to determine the range with Didymos during the ECP.[6]

In this work, we develop an autonomous optical navigation strategy which relies on a Convolutional Neural Network (CNN)-based IP algorithm that estimates the position of the COM of Didymos and the range with it, limiting the errors introduced by the irregular shape of the asteroid, the illumination conditions and the presence of Dimorphos in the images. Since it is not a direct mea-
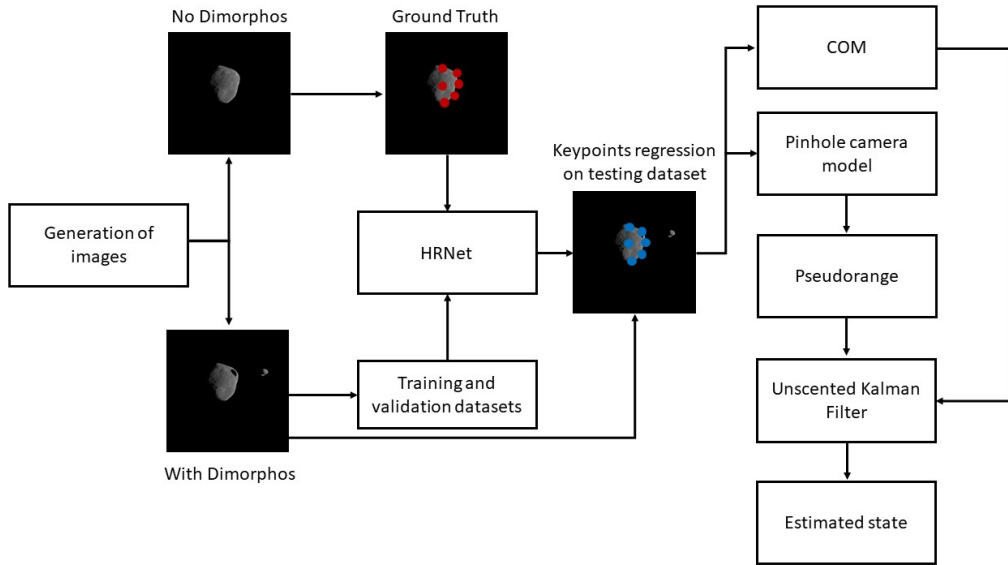
**Figure 1**: Overall pipeline of optical navigation algorithm

surement but it is derived from the images, the estimated range is a pseudorange measurement. An Unscented Kalman Filter (UKF) is then used to estimate the relative position of the spacecraft, by combining the range and the COM measurements together with the information given by the dynamics. The goal of this paper is to assess the performances of the navigation strategy by examining the accuracy of the provided measurements and by investigating the effectiveness of the navigation filter.

Recent years have seen an increase of the implementation of CNNs in space image processing. One of the main advantages of CNNs with respect to standard IP algorithms is the robustness over disturbances and adverse characteristics of the images. Most of the CNNs process the input image with a network typically consisting of a series of high-to-low resolution subnetworks. This process reduces the input's resolution, which is then recovered through a low-to-high process. With this procedure, extracted visual data have low spatial precision and accuracy that are important aspects for an autonomous attitude navigation system. Therefore, this works adopts the High-Resolution Network (HRNet) architecture to maintain a high-resolution representation through the whole network.[7] This process leads to a keypoints regression with superior spatial precision and higher accuracy.

This paper is structured as follows. The next section describes the framework of our methodology. The section after performs the numerical simulations and analyze the results obtained. Finally, the conclusion and the directions for future work are presented.

METHODOLOGY

In this Section, the methodology of this research is described. Figure 1 shows the main steps of the undertaken pipeline. With the ECP reference trajectory and the software Planet and Asteroid Natural scene Generation Utility (PANGU), two sets of images are generated, one without the presence of Dimorphos and one with both bodies. The former set is processed to retrieve the Ground Truth (GT) keypoints which are used to supervise the training and validation of the HRNet. The GT keypoints are 25 points selected from the projected surface of the primary on the image plane which includes
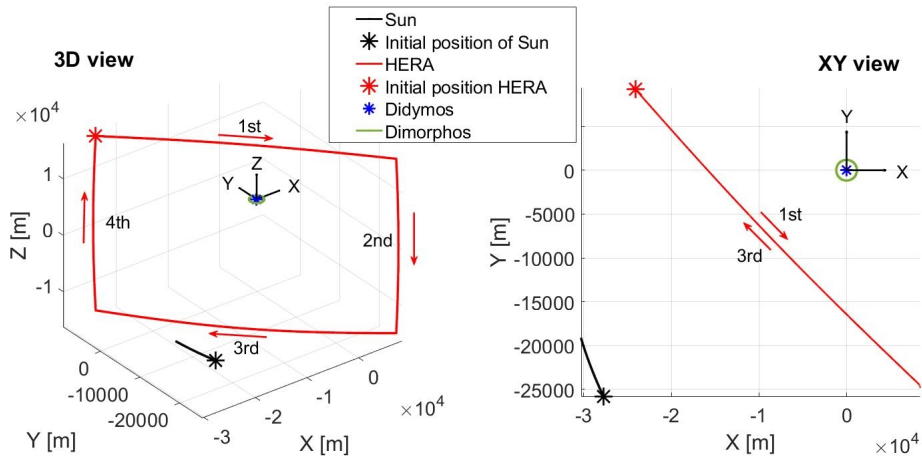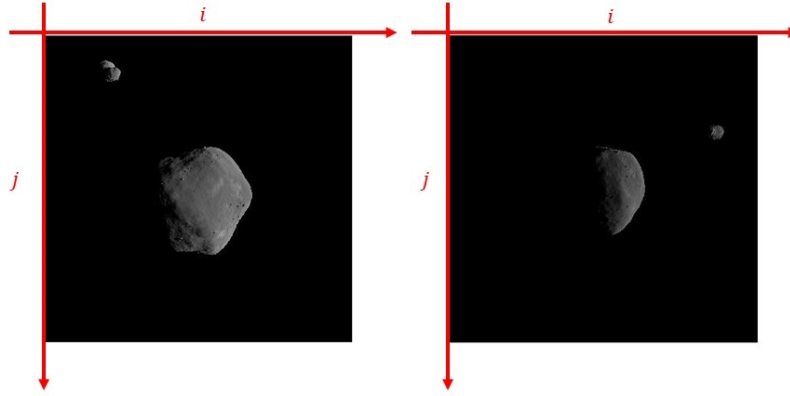
Figure 2: ECP trajectory
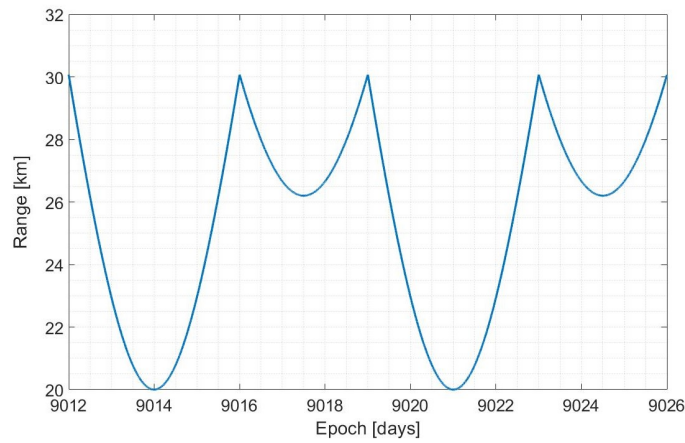
Figure 3: Range of the ECP trajectory

the COM and 24 points on the border. The second set of images is used for the training, validation and testing of the HRNet. The trained HRNet is applied to estimate the position of the keypoints of the testing dataset with both bodies. Then, the pinhole camera model is used with the estimated keypoints to measure the pseudorange. The latter is then coupled with the COM measurement to estimate the relative state of the spacecraft with respect to the binary asteroid system. Details of the main steps are described in the rest of this section.

Reference trajectory

The adopted reference frame is the Target Body Equatorial Inertial (TBEqI), which has the origin located on Didymos, the X-axis pointing towards the vernal equinox, and the XY plane coplanar to the equatorial plane of Didymos. The relative motion of the Sun around Didymos is retrograde as the binary system's orbit obliquity with respect to the Ecliptic plane is higher than $90°$, as shown in Table 1.

The ECP trajectory data is provided by ESA. Figure 2 represents the trajectory of the spacecraft, together with the position of the Sun (scaled down in the illustration) and the orbit of the secondary.

Figure 4: PANGU viewer with two sample images captured at different points of the ECP trajectory
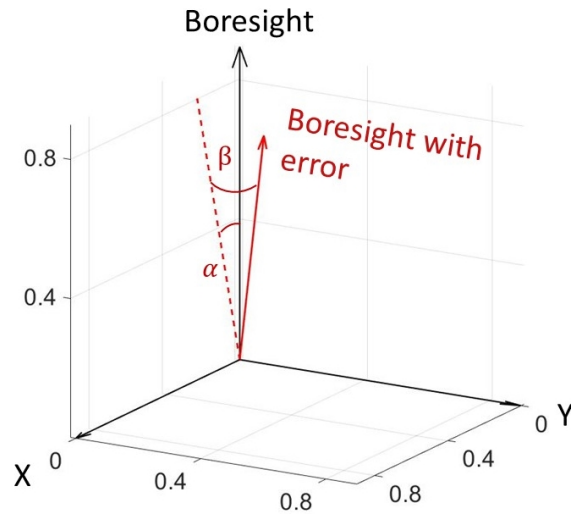
Figure 5: Camera pointing with error

The position of the Sun is calculated using the Jet Propulsion Laboratory Small Body Database.[8] The trajectory consists of 4 hyperbolic arcs, with an initial epoch of $t_{in} = 9012$ days and a final epoch of $t_{fin} = 9026$ days, calculated in the Modified Julian Date 2000. The only forces considered for each arc are the point mass gravitational attractions of both the primary and the secondary. Orbital manoeuvres are performed at the joint of two arcs. The duration of the 1st and 3rd arcs is 4 days while the duration of the 2nd and 4th arcs is 3 days. The range with respect to the primary varies between a minimum of $20\ km$ and a maximum of $30\ km$ as shown in Figure 3. It can be seen from Figure 2 that the ECP trajectory is interposed between the Sun and Didymos, in order to provide the AFC camera with bright images for the centroiding navigation.[4]

Generation of images

The software PANGU is used to generate the database of images for this work. PANGU is a simulation tool that models planet and asteroids surfaces and provides a high degree of realism in the visualization of images while operating at near real-time speeds. The software has been developed

by the STAR-Dundee engineering company.[9] The models of Didymos, Dimorphos and the camera are provided by GMV Aerospace and Defence, in charge of the GNC system of the HERA mission. Didymos' shape is near-spherical, and it is a spinning top with an elevated ridge along the equator. The shape of Dimorphos is not well known and it is approximated by scaling down the shape model of Itokawa that was the target asteroid of the Hayabusa mission. The software generates the images detected by the camera and shows them on the PANGU viewer, a plane with the size of the image (shown in Table 2) and the origin of the coordinated frame set to the top left corner. The horizontal and the vertical axes of the plane are referred as i-direction and j-direction respectively.

In order to visualize the binary system of asteroids on PANGU, the flight file system is operated. These files control the PANGU viewer and generate images taken at selected points of the reference trajectory in the TBEqI reference system, considering the position of the Sun (range, Azimuth and Elevation) and the positions and the orientations (quaternions) of both the binary asteroid system and of the AFC camera (joined with the spacecraft).[9]

During asteroid imaging, the AFC has its boresight pointing towards the primary and the vertical axis of the camera is perpendicular to the direction of the Sun with respect to HERA.[4] PANGU adopts the boresight, the vertical and the horizontal axis of the camera respectively as the Z- the Y- and the X-axis of the camera reference frame.[9] Therefore, the position vector of the Sun with respect to HERA lies on the XZ plane of the camera frame. As a result, the images generated on the PANGU viewer always represent the binary system illuminated from the right side. Figure 4 shows two sample images generated at different points of the ECP trajectories, together with the i- and the j-directions of the PANGU viewer.

When the camera is pointing perfectly towards the primary, the latter is displayed in the middle of the PANGU viewer. With these conditions, the Geometrical Center (GC) of the PANGU model of the primary, that is the arithmetic mean position of all the points belonging to the body, is located at the central pixel with the coordinates $(i, j) = (512, 512)$ $pixels$ in the PANGU viewer. Because of its near-spherical shape, the COM of the primary almost coincides with its GC. Since the images used in this work are all generated with PANGU, it is assumed that the GC of Didymos is its centroid. If the camera's boresight is always pointing perfectly towards the GC of the asteroid, its position on the PANGU viewer will always be $(i, j) = (512, 512)$ $pixels$ for each image. Training the CNN algorithm with a set of images with these characteristics will result in an issue of lacking label variability. To overcome this issue a pointing error represented by spherical coordinates and defined by two angles α and β is introduced at each point of the trajectory in the boresight direction of the camera reference system, as shown in Figure 5, so that the generated images are shifted from the central position of the PANGU viewer. In order to make sure that the asteroid is within the Field of View (FOV) of the AFC camera, random values within an interval of $[-1, 1]°$ are considered for both α and β at each epoch. With these values, the primary location is shifted around the viewer.

Pinhole camera model

The pinhole camera model is implemented in PANGU using the properties of the AFC camera, shown in Table 2.[11,12] In the pinhole camera model, also called perspective camera model, the camera aperture is considered as a point rather than a lens. Therefore, this model is used to achieve a first-order approximation of the relationship between the coordinates of a point X in the 3D space and its projection x onto the 2D image plane of the camera,[13] given by Eq. 1:

$$x = K[R|t]X \tag{1}$$
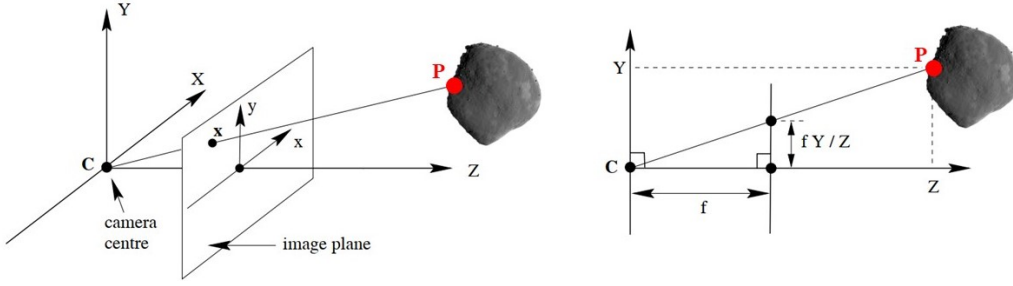
Figure 6: Pinhole camera model geometry[10]

Table 2: AFC properties[11,12]

FOV	Focal Length: f	Aperture	Image size	Pixel Size: ν
5.5°	10.6 cm	2.5 cm	$1024 \times 1024\ pixels$	14 μm

where K is the calibration matrix that depends on the intrinsic properties of the AFC camera and R and t are respectively the rotation matrix and the translation vector from TBEqI to the camera reference frame. Figure 6 shows the geometry of a pinhole camera model. In this model the centre of projection **C** is the origin of the camera reference frame and the image plane is located at the focal length $f = 10.6\ cm$ (Table 2). It can be seen from Figure 6, that a point in space **P** with coordinates (X, Y, Z) is mapped to a point on the image plane with the coordinates $(\frac{fX}{Z}, \frac{fY}{Z}, Z)$.[12] The units conversion from meters to pixels for an object of length l on the image plane is given by $n \cdot \nu\ pixels$, where n is the number of pixels representing the object and ν is the pixel size (Table 2). Therefore, an object of length L in meters on a plane of the 3D space at distance Z from the camera and parallel to the image plane is projected onto the latter with the dimensions in pixels defined by Eq. 2.

$$n \cdot \nu = \frac{f \cdot L}{Z} \tag{2}$$

Keypoints for the pseudorange

In order to apply the pinhole camera model to measure the pseudorange of the spacecraft with respect to Didymos, the shape of Didymos is approximated as a sphere of radius $R = 390\ m$ (Table 1). Given that on the image plane the length of the asteroid radius has a value of $n_R\ pixels$, Eq. 2 can be solved for Z, which is the distance from the centre of projection **C** and the COM of Didymos, i.e. the range. Therefore, once n_R of an image captured by the camera is obtained, the range can be calculated with Eq. 3.

$$Pseudorange = \frac{f \cdot R}{n_R \cdot \nu} \tag{3}$$

Figure 7a shows how n_R is calculated for a generic synthetic image of the asteroid, which is measured by the number of pixels from the COM to the point P on the asteroid's border along the i-direction. Dimorphos is hidden from the images as its presence in front of Didymos or near its border would disturb the evaluation of n_R.

Nevertheless, this calculation of n_R is highly dependant on the relative attitude of Didymos with respect to the spacecraft because of the asteroid's irregular shape. To reduce the error introduced

(a) Two points
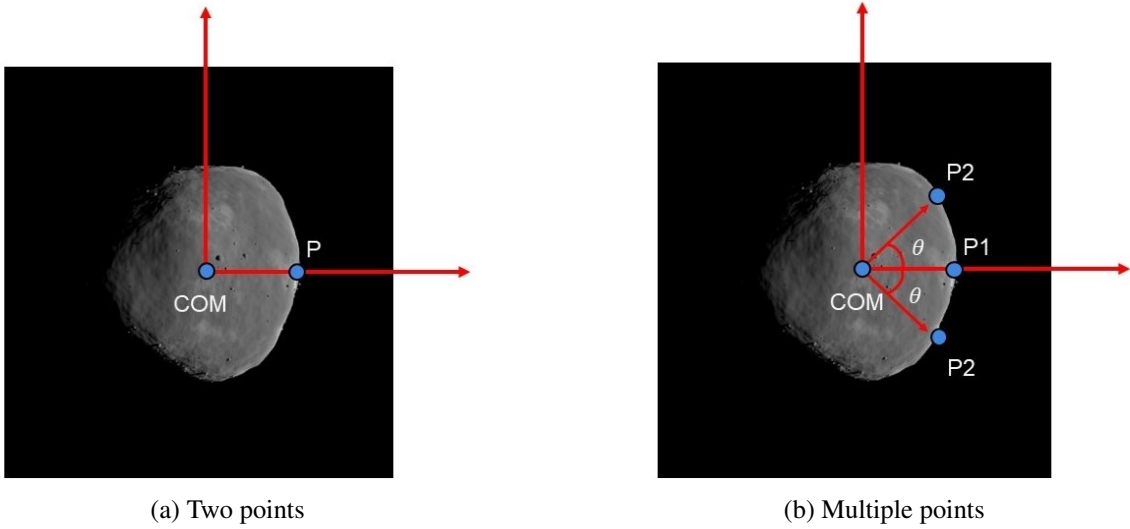
(b) Multiple points

Figure 7: Keypoints selected from the visible border of the asteroid
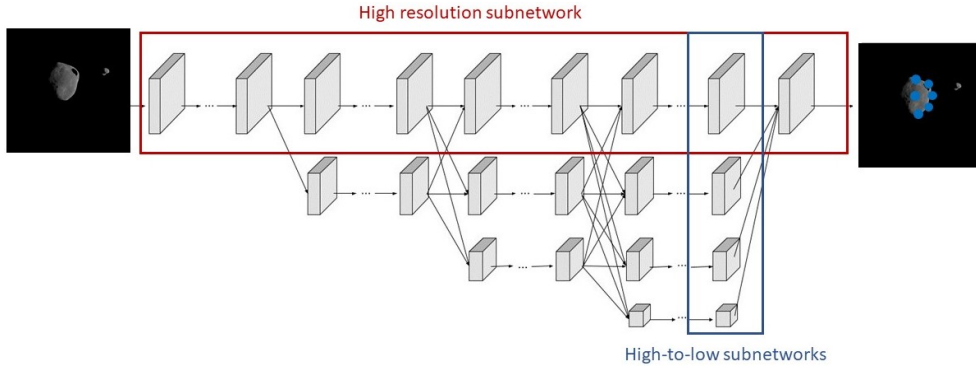
Figure 8: HRNet architecture

by the irregularity of the shape, multiple points P_i on the border within an arc of angular aperture 2θ are considered, as shown in Figure 7b. The distance n_R^i is evaluated for each point P_i and the average value $\bar{n}_R$ is calculated and used in Eq. 3 to measure the pseudorange. In this study we select 24 points P_i on the border within an arc of aperture 2θ with $\theta = 87°$.

HRNet

The HRNet architecture is shown in Figure 8. The network maintains the high resolution representations of the input images by connecting multiple subnetworks in parallel. The first stage is a high-resolution subnetwork. New stages are formed from the gradual introduction of high-to-low subnetworks. To maintain the high-resolution representation, repeated multiscale fusions are performed using low-resolution representation of the same depth and similar level. The last high-resolution representation is then used for the regression of the selected visual data.[7]

The keypoints to regress for each image are 25 points on the surface of Didymos, which are the COM and the 24 points on the visible border of the asteroid. Each input image of the HRNet is

coupled with the 25 corresponding keypoints that are used to supervise the training to regress the keypoints locations on the testing dataset. In this work, the pose-hrnet-w32 is used, where 32 represent the widths of the high-resolution subnetwork in the last three stages. During training, the validation dataset is used beside the training one to compute the validation losses and avoid overfitting. The Adam optimizer is used with a cosine decaying learning rate with initial value of 10^{-3} and decaying factor of 0.1. The total parameters involved in the training process are $28,536,377$.

The input dataset consists of 12104 (61.53%) images for training, 1513 (7.69%) for validation and 6052 (30.78%) for testing that are obtained by sampling the ECP trajectory respectively every 100, 800 and 200 seconds. Each image show both bodies, so that the HRNet is trained to regress the location of the keypoints despite the disturbance introduced by the presence of Dimorphos. The network is trained for 210 epochs.

Navigation filter

To combine the measurements produced by the image processing algorithm and form an accurate estimate of the state of the spacecraft, a navigation filter needs to be implemented. In this work, an Unscented Kalman Filter (UKF) is used for this purpose.[14] Compared with the Extended Kalman Filter (EKF), the UKF allows the full non-linear dynamics and measurement equations to be used, which results in an estimate of the posterior mean and covariance accurate up to the third order.[15] The following section discusses the implementation of this filter, the dynamics and measurement equations used, and the tuning of the filter for the specific problem of the ECP trajectory.

The UKF is based on a non-linear uncertainty propagation technique called the Unscented Transform (UT). Consider a non-linear function $\boldsymbol{y} = g(\boldsymbol{x})$, where $\boldsymbol{x}$ is a random variable with mean $\bar{\boldsymbol{x}}$ and covariance $P_{\boldsymbol{x}}$. The UT forms a matrix $\mathcal{X}$ consisting of a set of $2n + 1$ sigma points, where n is the size of the state vector $\boldsymbol{x}$, constructed as follows:

$$\mathcal{X}_0 = \bar{\boldsymbol{x}}$$
$$\mathcal{X}_i = \bar{\boldsymbol{x}} + (\sqrt{(n+\lambda)P_x})_i, \quad i = 1, ..., n$$
$$\mathcal{X}_i = \bar{\boldsymbol{x}} - (\sqrt{(n+\lambda)P_x})_i, \quad i = n+1, ..., 2n.$$

Here, $\lambda = \alpha^2(n + \kappa) - n$ is a tuning factor, and $(\sqrt{(n+\lambda)P_x})_i$ is the i-th row of the matrix $\mathcal{X}$. For the square root, the Cholesky decomposition technique is used. A set of sigma points are constructed from $\mathcal{X}$ and propagated through $g(\mathcal{X}_i)$ to obtain a set of propagated sigma points $\mathcal{Y}_i$. The mean and covariance can be formed from these points using the weights W_i as follows:

$$\bar{\boldsymbol{y}} \approx \sum_{i=0}^{2n} W_i^m \mathcal{Y}_i$$
$$P_{\boldsymbol{y}} \approx \sum_{i=0}^{2n} W_i^c (\mathcal{Y}_i - \bar{\boldsymbol{y}}) \cdot (\mathcal{Y}_i - \bar{\boldsymbol{y}})^T$$
$$W_0^m = \lambda/(n+\lambda)$$
$$W_0^c = \lambda/(n+\lambda) + (1 - \alpha^2 + \beta)$$
$$W_i^m = W_i^c = 1/(2n+\lambda), \quad i = 1, ..., 2n.$$

The benefit of this approach is the guarantee of accuracy up to third-order for the case of a Gaussian random variable, while minimizing the number of samples that need to be propagated through the

non-linear equations. The UKF implements the UT and changes the definition of the state $\boldsymbol{x}$ to the augmented state $\boldsymbol{x}^a = [\boldsymbol{x}^T, \boldsymbol{w}^T, \boldsymbol{v}^T]$, where $\boldsymbol{w}$ is the process noise and $\boldsymbol{v}$ is the measurement noise.

Compared to the UKF, the EKF is more computationally efficient as no samples need to be propagated and the linearized equations are used to propagate the estimated state. As the sampling rate of the measurements considered here is relatively slow, the accuracy of the UKF outweighs the numerical efficiency of the EKF, therefore the UKF is used for this case. The individual steps of the UKF are shown in algorithm 1.

Algorithm 1 The Unscented Kalman Filter

Initialize:

$\hat{\boldsymbol{x}}_0 = \mathbb{E}[\boldsymbol{x}_0]$

$P_0 = \mathbb{E}[(\boldsymbol{x}_0 - \hat{\boldsymbol{x}}_0) \cdot (\boldsymbol{x}_0 - \hat{\boldsymbol{x}}_0)^T]$

$\hat{\boldsymbol{x}}_0^a = \mathbb{E}[\boldsymbol{x}_0^a] = [\hat{\boldsymbol{x}}_0, \boldsymbol{0}, \boldsymbol{0}]$

$P_0^a = \begin{bmatrix} P_0 & & \boldsymbol{0} \\ & P_{\boldsymbol{w}} & \\ \boldsymbol{0} & & P_{\boldsymbol{v}} \end{bmatrix}$

for Each measurement $\boldsymbol{z}_k$ at time $k = 1, \ldots, t_f$ **do**

  Calculate sigma points from rows $\mathcal{X}_{k-1}^a$

  Update Step:

  $\mathcal{X}_{k|k-1}^x = \boldsymbol{f}(\mathcal{X}_{k-1}^x, \mathcal{X}_{k-1}^w)$

  $\hat{\boldsymbol{x}}_k^- = \sum_{i=0}^{2n} W_i^m \mathcal{X}_{i,k|k-1}^x$

  $P_k^- = \sum_{i=0}^{2n} W_i^c (\mathcal{X}_{i,k|k-1}^x - \hat{\boldsymbol{x}}_k^-) \cdot (\mathcal{X}_{i,k|k-1}^x - \hat{\boldsymbol{x}}_k^-)^T$

  $\mathcal{Z}_{k|k-1} = \boldsymbol{h}(\mathcal{X}_{k-1}^x, \mathcal{X}_{k-1}^v)$

  $\hat{\boldsymbol{z}}_k^- = \sum_{i=0}^{2n} W_i^m \mathcal{Z}_{i,k|k-1}$

  Measurement Step:

  $P_{\boldsymbol{z}_k,\boldsymbol{z}_k} = \sum_{i=0}^{2n} W_i^c (\mathcal{Z}_{i,k|k-1} - \hat{\boldsymbol{z}}_k^-) \cdot (\mathcal{Z}_{i,k|k-1} - \hat{\boldsymbol{z}}_k^-)^T$

  $P_{\boldsymbol{x}_k,\boldsymbol{z}_k} = \sum_{i=0}^{2n} W_i^c (\mathcal{X}_{i,k|k-1}^x - \hat{\boldsymbol{x}}_k^-) \cdot (\mathcal{Z}_{i,k|k-1} - \hat{\boldsymbol{z}}_k^-)^T$

  $K = P_{\boldsymbol{x}_k,\boldsymbol{z}_k} P_{\boldsymbol{z}_k,\boldsymbol{z}_k}^{-1}$

  $\hat{\boldsymbol{x}}_k = \hat{\boldsymbol{x}}_k^{-1} + K(\boldsymbol{z}_k - \hat{\boldsymbol{z}}_k^-)$

  $P_k = P_k^- - K P_{\boldsymbol{z}_k,\boldsymbol{z}_k} K^T$

end for

State and Measurement Dynamics

There are various options in terms of modelling the dynamics of the spacecraft. The main forces acting on the spacecraft are the gravitational forces from both Didymos and Dimorphos, the solar radiation pressure (SRP), and the third body gravitation of the Sun. To reduce the computational complexity, the main force to be included will be the gravitational attraction of the two bodies. At the distance of the ECP, it was found that for accurate modelling the point mass model is sufficient.[16] This setup does neglect certain unmodelled forces and thus it is important to reflect this in the design of the process noise. A technique called Dynamic Model Compensation (DMC)[17] is used, where an exponentially correlated bias acceleration is added to the dynamics. This acceleration is then used as a new parameter to be estimated at each time step by the navigation filter. As, in reality, most of the unmodelled accelerations are correlated in time, the dynamics of this parameter is modelled as
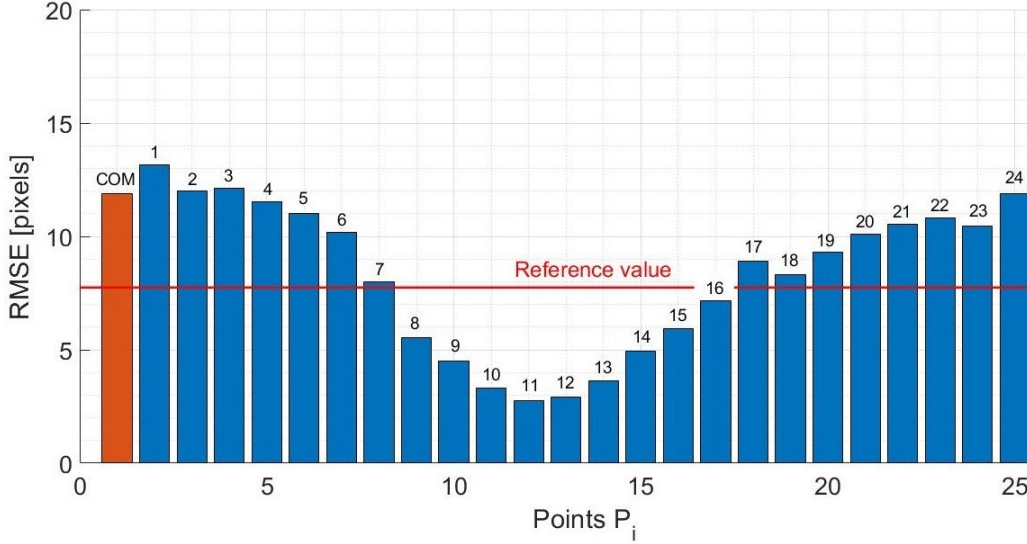
Figure 9: Accuracy of the keypoints regression

a first-order Gauss Markov process:

$$\boldsymbol{a}_{k+1} = e^{-\frac{dt}{\tau}} \boldsymbol{a}_k + \boldsymbol{\omega}(t), \tag{4}$$

where $\boldsymbol{a}$ is the bias acceleration, dt the filter time step, τ the autocorrelation parameter which determines the "smoothness" of the process, and $\boldsymbol{\omega}$ is a zero-mean Gaussian noise. The maneuvers to change the arcs of the ECP are not added into the dynamics, as the acceleration bias of Eq. (4) is expected to capture this as well. Future work will look more into different setups to include these maneuvers and improve the filter's performance.

For the measurement equation $\boldsymbol{z} = h(\boldsymbol{x})$, the sensor model of the camera for the COM and the range needs to be implemented. For the COM, the pinhole model discussed previously is used (Eq. 1). The rotation matrix R between the Didymos reference frame and the spacecraft frame at each point in time is assumed to be given by the attitude determination system. The range measurement equation is simply the norm of the spacecraft position vector given in:

$$\rho = \sqrt{x^2 + y^2 + z^2} \tag{5}$$

RESULTS

In this section, the results of the HRNet-based IP algorithm for the measurement of the pseudor-ange and the estimation of the COM position are presented. Firstly, the accuracy of the HRNet on the estimation of the positions of the 25 keypoints is analyzed with the metric defined as follows:

$$RMSE_m = \sqrt{\frac{\sum_{n=1}^{N}(P_{mn}^{GT} - P_{mn}^{Est})^2}{N}} \tag{6}$$

where P_{mn} represents the m-th 25 keypoint; the index n refers to the n-th image of the $N = 6052$ images of the testing dataset; $RMSE_m$ is the Root Mean Squared Error (RMSE) between the GT

11
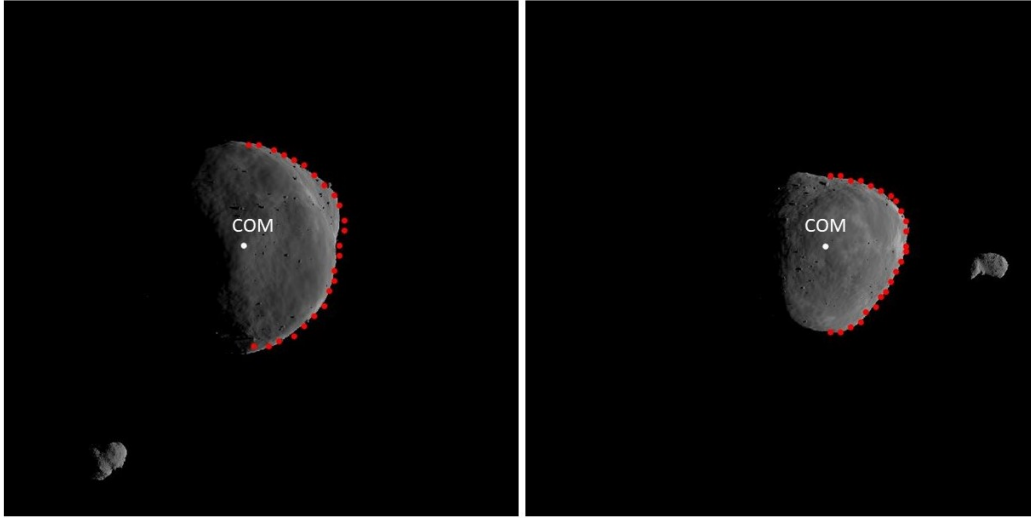
Figure 10: Keypoints regression results for two images of the 1st and the 3rd arc

position of the m-th keypoint P_{mn}^{GT} and the estimation P_{mn}^{Est} made by the HRNet. Eq. 6 is applied to all the 25 keypoints. To determine the accuracy of the keypoint regression, the $RMSE$ value obtained by the Maximum Correlation with a Lambertian Sphere (MCLS) IP algorithm developed by GMV Aerospace and Defence to estimate the position of the centroid of Didymos during the ECP of the HERA mission is given as a reference: $RMSE_{GMV} = 7.746 \; pixels$. This result is obtained by applying the algorithm over a set of 243 images generated during the ECP.

The accuracy of the results of the pseudorange is assessed through a metric defined by the percent error between the GT value and its estimation. The distribution of the percent error is also analyzed, since the optimality of navigation filters assumes the errors having a Gaussian distribution.

Accuracy of keypoints regression

Figure 9 is a bar chart of the $RMSE$ values obtained for the 25 keypoints regressed by the HRNet. The first bar represents the $RMSE$ for the COM position estimation. The other 24 points are located on the border of the asteroid. It can be seen that the worst performance of the HRNet is reached for the first point ($\theta = 87°$) of the border of the asteroid and the best performance for the 11th point, with values of the $RMSE$ equal to 13.161 $pixels$ and 2.973 $pixels$ respectively.

The difference on the estimation accuracy for each point is depending on the different lighting conditions and on the shape of the asteroid. Nevertheless, the $RMSE$ values are very close to the ones obtained by the MCLS IP algorithm. Therefore, the HRNet is able to estimate the position of the keypoints with high accuracy independently from the presence of Dimorphos and the irregular shape of the asteroid. Figure 10 shows 2 images generated by PANGU during the first and the third arc, together with the keypoints estimated by the HRNet.

Pseudorange measurement

Figure 11 shows the results obtained for the pseudorange estimation with the HRNet-based IP algorithm. The plot above shows that the estimation is similar to the ground truth illustrated in Figure 3. The plot below in Figure 11 shows that the absolute percent error is lower than 10% and
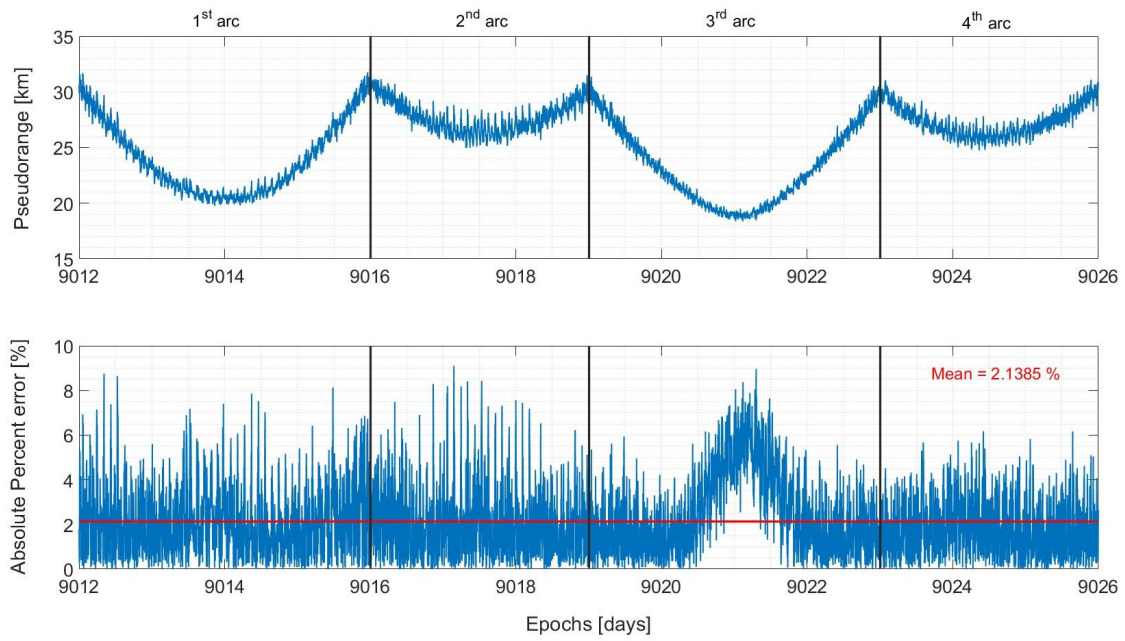
Figure 11: Pseudorange estimation
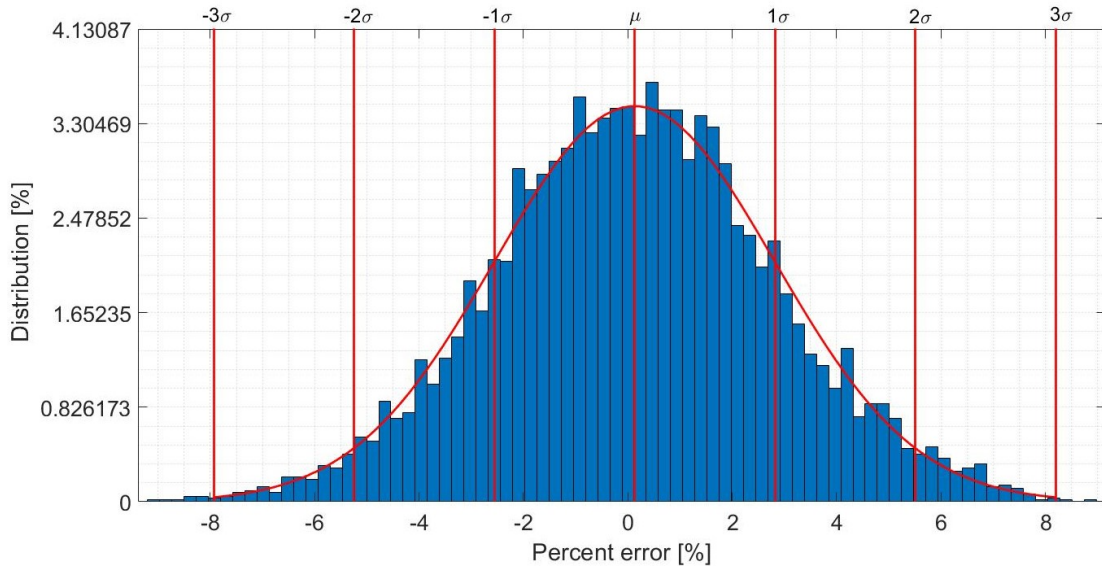
Figure 12: Pseudorange percent error distribution

it oscillates around a mean value of 2.1385%. It can be seen that when the range reaches its local minima in the 1st and 3rd arcs, the absolute percent error is higher, due to the fact that the images of the asteroid are appearing larger in the image plane. As a consequence, the non-spherical shape becomes more predominant and the approximation as a sphere is less accurate.

Figure 12 represents the distribution of the percent error of the pseudorange estimation, which is similar to a white noise with the mean value of $\mu = 0.1298\%$ near 0. It means that the designed
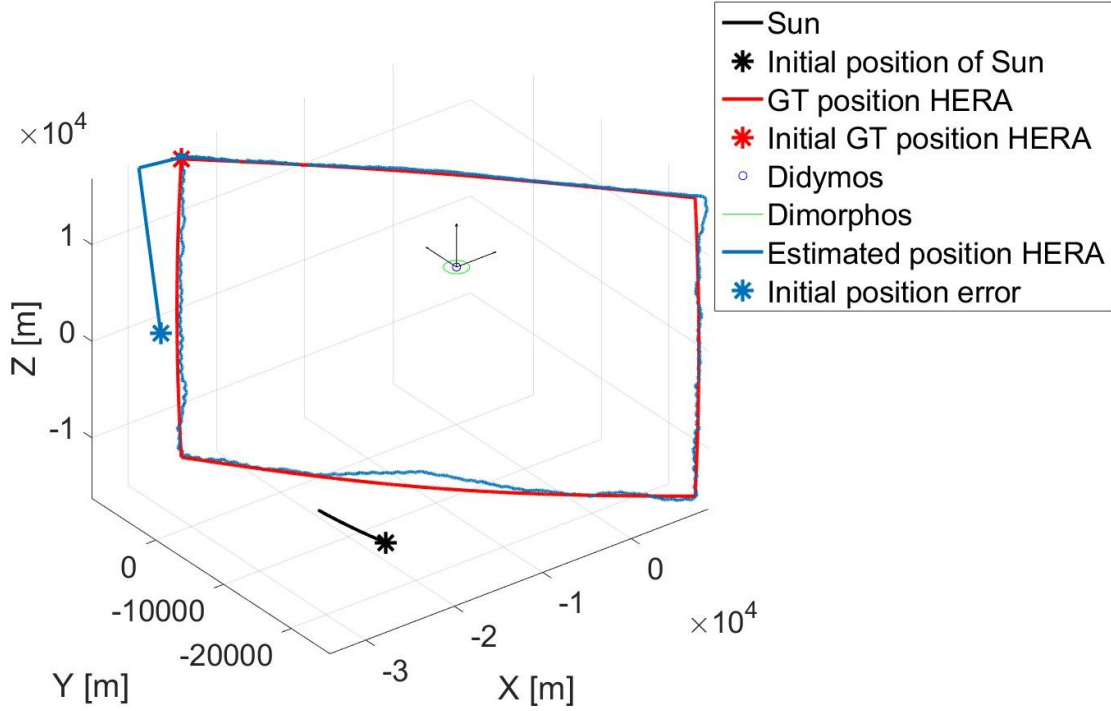
Figure 13: The difference between the true ECP trajectory and the estimated one.

algorithm does not suffer from any systematic errors. The value of the error that occurs the most, which is represented by the highest peak of the histogram, is 0.4695%. The standard deviation of the error is $\sigma = 2.6888\%$ which means that 68.27% of the pseudorange measurements have a percent error ranging between -2.559% and 2.8186% with respect to the ground truth. The distribution of the error is symmetrical ($skewness = 0.0176$) and light-tailed ($kurtosis = 3.0067$) which means that the percent error distribution is similar to a Gaussian distribution.
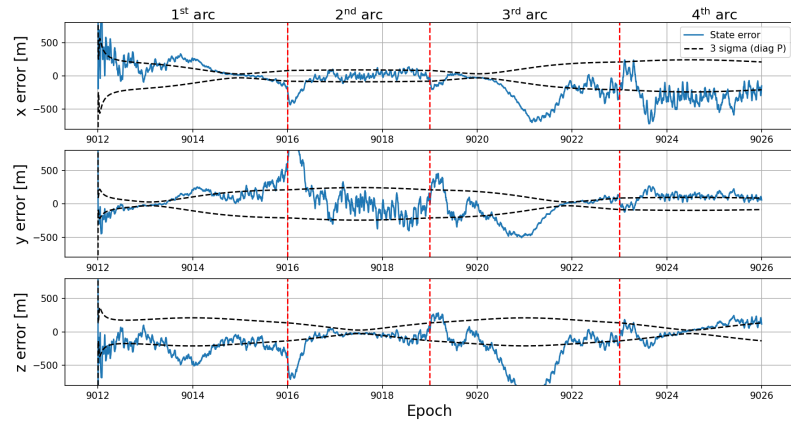
Navigation Filter

An error of $10\ km$ and $0.1\ m/s$ is introduced in the initial estimate of the state, while the initial estimate of the acceleration bias is $0\ m/s^2$. The settings of the filter matrices is given in Table 3. The estimated trajectory resulting from the navigation filter is shown in Figure 13, and the errors in the state variables are shown in Figure 15 in the TBEqI. The initial error in the state estimate quickly decreases in the 1st arc and results in final estimates below around $300\ m$ for the position and 0.5 cm/s for the velocity. As the second arc starts, the error increases quickly as the acceleration bias estimate, seen in Figure 15c, needs to correct for the unmodelled ΔV acceleration before the filter corrects it again. This happens again for the 3rd and 4th arcs. The effect of the spacecraft maneuvers can be seen more significantly in the velocity error in Figure 15b, as the velocity estimate is mainly determined through the dynamics update of the filter and less by the input of the measurements. However, for both the position and velocity, the filter is able to quickly decrease the errors to the values mentioned before as more measurements come in. This shows the capability of the filter to react to unmodelled accelerations like the maneuvers of the spacecraft and keep the navigation error low.

Table 3: The settings of the navigation filter

Variable	Value	Unit
$P_{0,r}$	1000^2	m
$P_{0,v}$	0.1^2	m/s
$P_{0,a}$	0.0001^2	m/s^2
Q_r	0	m
Q_v	$1e-6$	m/s
Q_a	$1e-8$	m/s^2
$R_{u,cam}$	15^2	pixels
$R_{v,cam}$	10^2	pixels
R_ρ	500^2	m
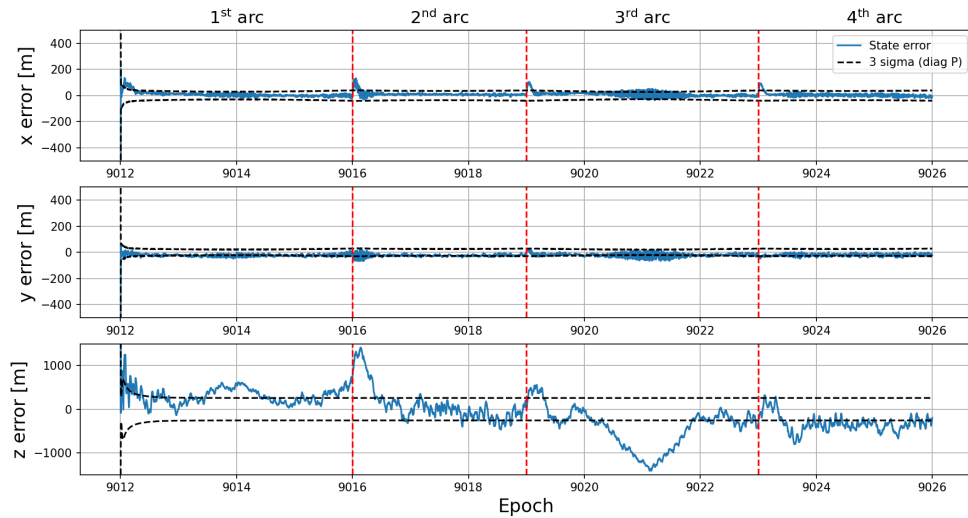
Figure 14: The difference between the true ECP trajectory and the estimated one in the camera reference frame

The main component that is affecting the overall accuracy of the position estimate is the measurement of the range with respect to Didymos. Figure 15a shows in the 3rd arc a large region where the error increases, which is caused by the decrease in accuracy of the range error shown in Figure 11. The state errors are transformed to the camera reference frame, where the z-axis points towards the center of Didymos, as is shown in Figure 14. This shows more clearly that the majority of the error comes from the radial direction, as the x- and y-direction have significantly smaller errors compared to the z-direction. Therefore, improving the measurement of the range will have a large impact on the general accuracy of the navigation system.

(a) Position errors in TBEqI
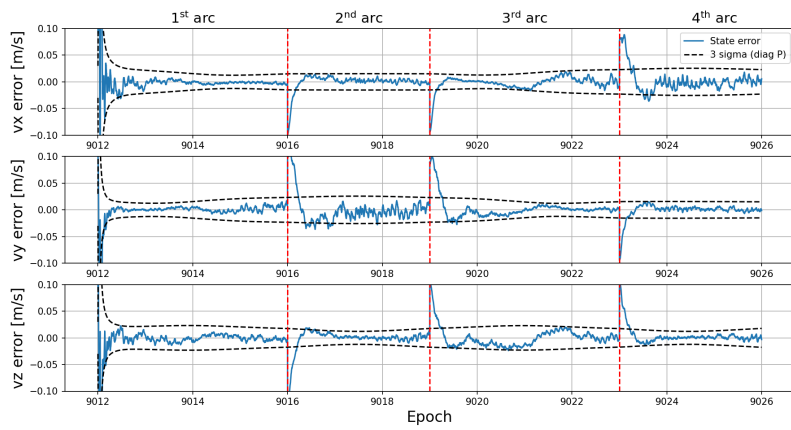
(b) Velocity errors in TBEqI
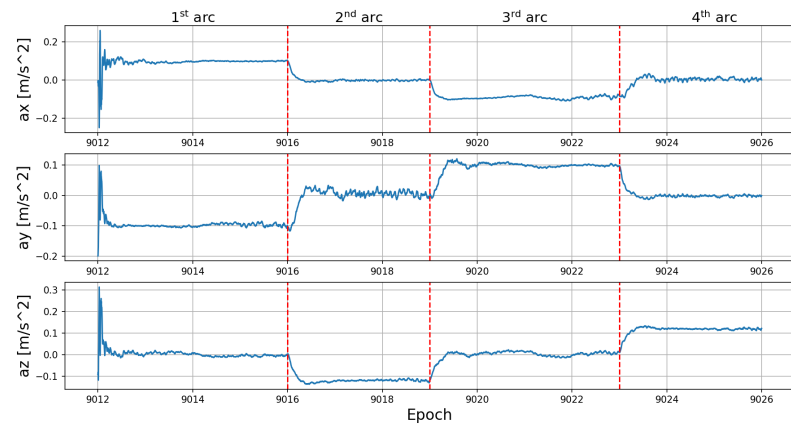
(c) Acceleration bias estimates.

Figure 15: The results for the navigation filter using the HRNet-based image processing measurements

CONCLUSION

This paper develops a CNN-based IP algorithm addressing the state estimation problem for autonomous optical navigation around a binary asteroid system. The ECP proximity operation of the HERA mission to Didymos system is studied as case scenario. The main objective of the developed methodology is to provide the navigation algorithm with the asteroid COM and pseudorange measurements that support the state (position and velocity) estimation of the spacecraft and increase the robustness of the navigation algorithm. The training, validation and testing datasets of images are generated using the software PANGU with the ECP reference trajectory. The chosen CNN architecture is the HRNet, that is the state of the art in keypoint detection and that has been already exploited for space applications. The navigation filter we used is a UKF.

The results show that the HRNet-based IP algorithm is able to measure the COM position and the pseudorange with high accuracy and the methodology is robust to the disturbances caused by the irregular shape of the asteroid and the presence of Dimorphos. In particular the percent error of the range has a near-Gaussian distribution, which is ideal for navigation filters. The UKF performs well by estimating the state with high accuracy. Future work would go into the direction of other utilizations for the HRNet-based IP algorithm. For instance, and additional estimated output that is useful for the navigation algorithm of the GNC system during the proximity operations with the asteroid is the pose estimation of Didymos.

ACKNOWLEDGMENT

REFERENCES

[1] P. Michel, A. Cheng, and M. Küppers, "Asteroid Impact and Deflection Assessment (AIDA) mission: science investigation of a binary system and mitigation test," *European Planetary Science Congress*, Nantes, France, pp. 123–124. October, 2015.

[2] P. Michel, I. Carnelli, and M. Küppers, "The Hera mission: European component of the ESA-NASA AIDA mission to a binary asteroid," *COSPAR Scientific Assembly*. 2018.

[3] ESA Headquarters, *HERA Didymos reference model*, 2021.

[4] ESA Estec, *HERA: Proximity Operations Guidelines*, 2020.

[5] A. Pellacani, M. Graziano, M. Fittock, J. Gíl-Fernández, and I. Carnelli, "HERA vision based GNC and autonomy," *European Conference for AeroSpace Sciences*, 2019, pp. 1–14.

[6] N. G. Dias, P. Gordo, H. Onderwater, R. Melicio, and A. Amorim, "Analysis on the Isostatic Bipod Mounts for the HERA Mission LIDAR," *Applied Sciences (Switzerland)*, Vol. 12, No. 7, 2022, 10.3390/app12073497.

[7] K. Sun, B. Xiao, L. Dong, and J. Wang, "Deep high-resolution representation learning for human pose estimation," *Proceedings of the IEEE Computer Society Conference on Computer Vision and Pattern Recognition*, pp. 5686–5696. June, 2019.

[8] NASA, "JPL Solar System Dynamics," 2021.

[9] Dundee University, *Planet and Asteroid Natural Scene Generation Utility User Manual*, 2019.

[10] R. Hartley and A. Zisserman, "Camera Models," *Physically Based Rendering*, 2004, pp. 153–177, 10.1016/b978-0-12-375079-2.50006-8.

[11] ESA, "Hera mission instruments," 2021.

[12] H. Sierks, H. U. Keller, R. Jaumann, H. Michalik, T. Behnke, F. Bubenhagen, I. Büttner, U. Carsenty, U. Christensen, R. Enge, B. Fiethe, P. Gutiérrez Marqués, H. Hartwig, H. Krüger, W. Kühne, T. Maue, S. Mottola, A. Nathues, K. U. Reiche, M. L. Richards, T. Roatsch, S. E. Schröder, I. Szemerey, and M. Tschentscher, *The Dawn framing camera*, Vol. 163. 2011, 10.1007/s11214-011-9745-4.

[13] P. Sturm, *Pan-Tilt-Zoom (PTZ) Camera*. 2021, 10.1007/978-3-030-63416-2472.

[14] S. J. Julier and J. K. Uhlmann, "Unscented Filtering and Nonlinear Estimation," *Proceedings of the IEEE*, Vol. 92, 2004, pp. 401–422.

[15] E. A. Wan and R. V. D. Merwe, "The unscented Kalman filter for nonlinear estimation," Institute of Electrical and Electronics Engineers Inc., 2000, pp. 153–158, 10.1109/ASSPCC.2000.882463.

[16] F. Ferrari, V. Franzese, M. Pugliatti, C. Giordano, and F. Topputo, "Trajectory Options for Hera's Milani CubeSat Around (65803) Didymos," *The Journal of the Astronautical Sciences*, 9 2021, pp. 1–22, 10.1007/S40295-021-00282-Z.

[17] N. Stacey and S. D'Amico, "Adaptive and Dynamically Constrained Process Noise Estimation for Orbit Determination," *IEEE Transactions on Aerospace and Electronic Systems*, Vol. 57, 10 2021, pp. 2920–2937, 10.1109/TAES.2021.3074205.